Oxygen reduction reaction of PrBaCo2-xFexO5+d compounds as H+-SOFC cathodes : correlations with physical properties

Alexis Grimaud, Jean-Marc. Bassat, Fabrice Mauvy, Michaël Pollet, Alain Wattiaux, Mathieu Marrony, Jean-Claude Grenier

▶ **To cite this version:**

Alexis Grimaud, Jean-Marc. Bassat, Fabrice Mauvy, Michaël Pollet, Alain Wattiaux, et al.. Oxygen reduction reaction of PrBaCo2-xFexO5+d compounds as H+-SOFC cathodes : correlations with physical properties. Journal of Materials Chemistry A, 2014, 2 (10), pp.3594-3604. 10.1039/c3ta13956e . hal-00956730

HAL Id: hal-00956730
https://hal.science/hal-00956730

Submitted on 8 Jun 2022

HAL is a multi-disciplinary open access archive for the deposit and dissemination of scientific research documents, whether they are published or not. The documents may come from teaching and research institutions in France or abroad, or from public or private research centers.

L'archive ouverte pluridisciplinaire **HAL**, est destinée au dépôt et à la diffusion de documents scientifiques de niveau recherche, publiés ou non, émanant des établissements d'enseignement et de recherche français ou étrangers, des laboratoires publics ou privés.

Oxygen reduction reaction of $PrBaCo_{2-x}Fe_xO_{5+\delta}$ compounds as H+-SOFC cathodes : correlations with physical properties†

A. Grimaud,[a] J.-M. Bassat,[b] F. Mauvy,[a] M. Pollet,[a] A. Wattiaux,[a] M. Marrony[b] and J.-C. Grenier*[a]

$PrBaCo_{2-x}Fe_xO_{5+\delta}$ solid solution is investigated in order to understand the Oxygen Reduction Reaction (ORR) and water formation occurring at the H^+-SOFC cathode. Careful attention is paid to the study of the physical properties as a function of composition by Thermogravimetry Analysis (TGA), Mössbauer spectroscopy, electrical conductivity and Seebeck coefficient measurements, with the aim to establish the correlation existing with the ORR activity for these Mixed Ionic Electronic Conductors (MIEC). The oxygen diffusion coefficients are determined by Electrical Conductivity Relaxation (ECR) and Isotopic Exchange Depth Profile (IEDP) coupled with Secondary Ion Mass Spectroscopy (SIMS) methods. An electrochemical study is then carried out and shows that the amount of oxygen vacancies is the most influential parameter. Indeed, it allows some hydration of $PrBaCo_2O_{5+\delta}$ oxide and the formation of protonic defects that can induce protonic diffusivity in these MIEC oxides.

Introduction

Currently, Solid Oxide Fuel Cell (SOFC) devices suffer from the high operating temperature ($T \sim 800$ °C) required to obtain suitable efficiency by cogeneration. This leads to degradation issues and increases the cost of materials.[1] Solid oxide fuel cells based on protonic conducting electrolytes, so called H^+-SOFC in opposition to SOFC based on O^{2-} conduction, can operate in the temperature range of 400 to 600 °C thanks to the low activation energy of proton diffusion in comparison with oxygen diffusion.[2,3] Thus, it can represent an interesting alternative to SOFC technology. Among the remaining drawbacks concerning this technology, the high cathodic overpotential associated with oxygen reduction and water formation remains unsolved. To overcome this problem and design new electrode materials, a better understanding of the electrochemical process is of great interest. Indeed, the use of Mixed Ionic (O^{2-}) Electronic (e^-) Conductors (MIEC), commonly used as O^{2-}-SOFC cathodes, leads to a two step reaction:

$$\frac{1}{2}O_{2(g)} + 2e^- \rightarrow O^{2-} \quad (1)$$

$$2H^+ + O^{2-} \rightarrow H_2O_{(g)} \quad (2)$$

where the Oxygen Reduction Reaction ORR (1) takes place all over the gas/electrode interface and the water formation (2) occurs at the internal electrolyte/electrode interface. In addition to slow kinetics, severe degradations of the cathode layer during operation can arise from water formation at the internal interface.[4] This can be solved by developing mixed protonic (H^+) electronic (e^-) conductors, which enable the proton transfer from the electrolyte to the electrode and a one-step reaction, potentially with faster kinetics:

$$\frac{1}{2}O_{2(g)} + 2e^- + 2H^+ \rightarrow H_2O_{(g)} \quad (3)$$

Various strategies were adopted to develop MIEC (H^+/e^-) cathodes, such as the use of composite protonic conductor/MIEC (O^{2-}/e^-) oxide electrodes,[5,6] the substitution of protonic conductors with a transition metal to enlarge their electronic conduction[7,8] or the use of MIEC (O^{2-}/e^-) electrodes with a large amount of oxygen vacancies to allow hydration upon water partial pressure pH_2O and enable protonic conduction in the structure.[9–11]

Considering that oxygen vacancies are released during the water formation at the H^+-SOFC cathode through the relationship

$$2OH_O^{\cdot} \rightarrow H_2O_{(g)} + O_O^{\times} + V_O^{\cdot\cdot} \quad (4)$$

and are required at the surface of the electrode to allow the oxygen reduction:

[a]CNRS, Université de Bordeaux, ICMCB, 87 avenue du Dr. A. Schweitzer, Pessac, F-33608, France. E-mail: grenier@icmcb.bordeaux.cnrs.fr

[b]EIfER, Emmy-Noether-Strasse 11, Karlsruhe, D-76131, Germany

† Electronic supplementary information (ESI) available: Description of the electrical conductivity relaxation data fitting, chemical diffusion and thermodynamic factor, oxygen mobility and ionic conductivity calculation, elementary steps of the oxygen reduction reaction, XRD, SIMS data, SEM and impedance diagram fitting. See DOI: 10.1039/c3ta13956e

$$\frac{1}{2}O_{2(g)} + 2e^- + V_O^{\cdot\cdot} \rightarrow O_O^{\times} \quad (5)$$

the oxygen mobility can also be a limiting factor for H^+-SOFC electrodes. In this peculiar case, ORR and water formation do not necessarily occur at the same place but are strongly linked by the surface diffusion of oxygen vacancies. Thus, the use of triple protonic (H^+) ionic (O^{2-}) electronic (e^-) conductors could result in faster electrode kinetics compared to mixed (H^+/e^-) conductors, leading to interesting electrochemical performances.

Recently, we have studied the Rate Determining Steps (RDS) of the ORR of four MIEC (O^{2-}/e^-) oxides, $La_{0.6}Sr_{0.4}Fe_{0.8}Co_{0.2}O_{3-\delta}$, $Ba_{0.5}Sr_{0.5}Co_{0.8}Fe_{0.2}O_{3-\delta}$, $PrBaCo_2O_{5+\delta}$ and $Pr_2NiO_{4+\delta}$,[12] well-known for their good electrocatalytic properties. Even though it was demonstrated that a proton is involved in the oxygen reduction process and that hydration enhances the electrochemical performances of three of these MIEC oxides ($Ba_{0.5}Sr_{0.5}Co_{0.8}Fe_{0.2}O_{3-\delta}$, $PrBaCo_2O_{5+\delta}$ and $Pr_2NiO_{4+\delta}$), the chemical origin of this enhancement remained unclear. Following the work done by Peng *et al.*[6] demonstrating the role of electrical conductivity in the ORR at the H^+-SOFC cathode, the study of the $Pr_{2-x}Sr_xNiO_{4+\delta}$ solid solution thereafter highlighted that a key parameter concerning these over-stoichiometric oxides belonging to the Ruddlesden–Popper series is their ability to insert either additional oxygen or hydroxyl groups in the interstitial position, thanks to their structure flexibility.[13] We aim to extend this strategy in this work to the oxygen deficient double perovskite $PrBaCo_2O_{5+\delta}$ which has comparable performances to the H^+-SOFC cathode.[12] It is well known, for MIEC oxides, that the modification of the transition metal–oxygen bond by cationic substitution highly influences their physical properties such as electrical conductivity, oxygen content and evolution *vs.* temperature.[14] For instance, the important role of mobile oxygen vacancies was clearly emphasized in the case of BSCF-type O^{2-}-cathodes, not only for the oxygen transport in the bulk as expected, but also for the incorporation reaction at the surface.[14] A high oxygen vacancy concentration and mobility could then serve as a guideline in the search for alternative O^{2-} cathodes and also hopefully for H^+-cathode materials. The solid solution $PrBaCo_{2-x}Fe_xO_{5+\delta}$ with $x = 0$, 0.5, 1 and 1.5 was prepared with the aim to further understand the relationship existing between physical properties and electrochemical performances of H^+-SOFC cathodes.

The first part of this work is devoted to detailing the modifications of physical properties, such as structural features, cationic ordering, oxygen content and exchange with the atmosphere, electrical transport properties, oxygen surface exchange and diffusion coefficients induced by the transition metal substitution in $PrBaCo_2O_{5+\delta}$. Then, the electrochemical behaviour of these materials is studied: the rate determining steps are determined by electrochemical measurements carried out under high water partial pressure (pH_2O) and different oxygen partial pressure (pO_2). Finally, a tentative correlation between physical and electrochemical properties is suggested.

Experimental section

$PrBaCo_{2-x}Fe_xO_{5+\delta}$ ($x = 0$, 0.5, 1, 1.5 and 2) compounds were prepared by the modified Pechini method. The required amounts of high purity Pr_6O_{11}, $BaCO_3$, Co and Fe were thoroughly dissolved in nitric acid solution, then citric acid was added in 10% excess. The solution was dehydrated and slowly heated until the self-combustion. Submicronic particles were obtained and fired at 1100 °C for 10 hours for $PrBaCo_2O_{5+\delta}$ and 1200 °C for 12 hours for $PrBaCo_{2-x}Fe_xO_{5+\delta}$ ($x = 0.5$, 1, 1.5 and 2). Powders were characterized by X-ray diffraction performed on a PANanalytical X'pert MPD diffractometer using Bragg–Brentano geometry.

Mössbauer spectroscopy has been used to study the oxidation state and coordination of iron cations. The experiments were performed at room temperature in transmission geometry with a constant acceleration spectrometer using a ^{57}Co source in a Rh matrix. The velocity was calibrated by using pure iron metal as the standard material at room temperature. All isomer shifts reported in this work refer to the natural α-Fe at 293 K. All the spectra were recorded in a small range of velocity (-4 mm s^{-1}; +4 mm s^{-1}). The fraction of iron present in the structure was determined assuming equal recoil-free factor (f) for each of the ^{57}Fe nuclei in the structure.

Thermogravimetric analyses (TGA) were carried out on a TA Instrument TGAQ50 device in the temperature range 20–1000 °C at 1 °C min^{-1} rate in order to determine the thermal dependence of the oxygen content at a given pO_2, which is achieved by mixing oxygen and nitrogen using two mass flow controllers.

$PrBaCo_2O_{5+\delta}$ ($x = 0$) powder was isostatically pressed at 3000 bar for 10 min and sintered at 1300 °C for 12 hours. For $x \neq 0$, $PrBaCo_{2-x}Fe_xO_{5+\delta}$ powder was isostatically pressed at 2500 bar for 10 min and sintered at 1340 °C for 12 hours. Densities above 94% of the theoretical ones were obtained. The electrical conductivity was measured with the four-probe method in the 100–800 °C range while thermoelectric power measurements were carried out in the 25–800 °C range with homemade equipment previously described.[15]

Oxygen diffusion (D^*) and surface exchange coefficients (k^*) were determined on carefully polished dense pellets using the so-called IEDP (Isotopic Exchange – $^{18}O/^{16}O$ – Depth Profile) coupled with SIMS (Secondary Ion Mass Spectroscopy) analyses method. Prior to the isotopic exchange, the pellets were carefully polished and then thermodynamically equilibrated in a quartz tube, under a partial pressure (0.21 atm) of natural oxygen (99.75% ^{16}O) by annealing at a given temperature for about 10 times the duration of the exchange. The atmosphere is then replaced by ^{18}O (Eurisotop, 97%) and the pellets are annealed at the same temperature and pressure and then quenched. The ^{18}O diffusion profiles were recorded using a Cameca® IMS 6F device with a source of incident Cs^+ ions. The surface of exchanged pellets was scanned and ^{59}Co, ^{16}O and ^{18}O were mapped on a 250 × 250 μm^2 area. The normalized oxygen ^{18}O diffusion profile is then fitted using a model proposed by Crank,[16] for a solution of the second Fick law of gas diffusion in a solid. Further details can be found in previous studies.[17,18]

Electrical conductivity relaxation (ECR) measurements were carried out using the four probe method under a dry atmosphere. The pO_2 surrounding the sample was alternatively switched between 0.21 and 0.01 bar by means of a mixture of oxygen and nitrogen controlled by flow meters into a sample chamber. These pO_2 are sufficiently close to consider that the charge carrier mobility is constant and that the equilibrium time in the chamber is negligible (~30 seconds).[19–23] In a previous work concerned with $La_{0.5}Sr_{0.5}CoO_{3-\delta}$, the oxygen exchange kinetics was found to have a linear behaviour for a pO_2 ratio ≤20.[24] The pO_2 ratio used in this study is in the upper limit of this linear model.

Based on the Crank model,[16] the ratio $\frac{M_t}{M_\infty} = \frac{\sigma_t - \sigma_0}{\sigma_\infty - \sigma_0}$, σ_t, σ_0 and σ_∞ being the conductivity values at t, $t = 0$ and $t = \infty$, respectively, was fitted (see the ESI†), which allowed the calculation of k_{Chem} and D_{Chem}, the chemical surface exchange and diffusion coefficients, respectively.

For the electrochemical characterization experiments, commercial $BaCe_{0.9}Y_{0.1}O_{3-\delta}$ (BCY10) electrolyte powder (Marion Technologies) was isostatically pressed at 3000 bars for 10 min followed by sintering at 1400 °C for 10 hours to form pellets with density higher than 95%. Inks for screen printing electrodes were made by adding attrited powder (70% in mass) with particle sizes in between 0.4 and 0.8 μm in a terpineol medium. Cathodes were deposited on both sides of BCY10 dense pellets and sintered to obtain symmetrical half-cells. The microstructure of the electrodes was observed by Field emission Scanning Electron Microscopy (SEM) using a Jeol JSM 6330F.

Electrochemical Impedance Spectroscopy (EIS) measurements were performed using an Autolab PGStat 308 Frequency Response Analyser and an electrochemical cell equipped with a controlled gas humidification rate obtained by bubbling gas (1 bar) into a water tank maintained at a steady temperature leading to a given pH_2O. Equilibration time of two hours was required prior to the EIS acquisition between each atmosphere to insure thermodynamic stability. Impedance diagrams were fitted using Zview™ software (Scribner Associates).

Results and discussion

Structural characterizations

The synthesis of $PrBaCo_{2-x}Fe_xO_{5+\delta}$ samples with $x = 0$, 0.5, 1 and 1.5 compositions was performed in air, at 1200 °C. Single phases showing the typical perovskite XRD diagram were obtained, as seen in Fig. 1a. However, some additional peaks assigned to perovskite impurity (S.G. *Pbnm*) were observed for $PrBaFe_2O_{5+\delta}$, as already reported for similar compounds with high iron concentration $x > 1.5$.[25] For $x \leq 1$, the (110) perovskite diffraction peak splits into (110) and (102) peaks, which is characteristic of (001) planes alternatively occupied by alkaline earth (Ba) and rare earth (Pr) metals in which oxygen vacancies are mainly located (Fig. 1b). For higher iron content ($x > 1$), perovskites with a cubic structure are obtained, which denotes the loss of ordering of Ba and Pr cationic planes and consequently, of the oxygen vacancies. Interestingly, a sintering temperature of 1100 °C did not induce the ordering of any iron containing compounds (*cf.* ESI Fig. S1†). Space groups and lattice parameters of these compounds are summarized in Table 1. The substitution of Co by Fe results in an increase of the lattice volume in agreement with their ionic radii ($r_{Co^{3+}} = 0.61$, $r_{Co^{4+}} = 0.53$, $r_{Fe^{3+}} = 0.645$ and $r_{Fe^{4+}} = 0.585$ Å HS in 6-fold coordination).[26]

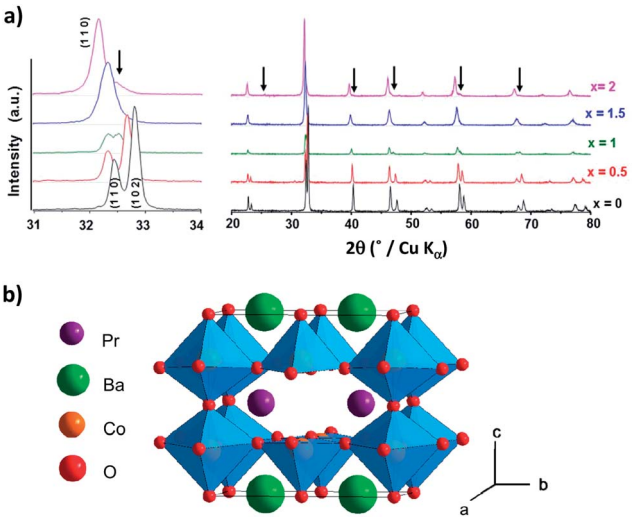

Fig. 1 (a) XRD diagrams of $PrBaCo_{2-x}Fe_xO_{5+\delta}$ compounds sintered in air, at 1000 °C for $x = 0$ and at 1200 °C for $x = 0.5$ to 2. The asterisk denotes an unknown impurity and arrows a secondary perovskite phase. (b) Structure of the double perovskite $PrBaCo_2O_{5+\delta}$ showing the ordering of the BaO and PrO_δ planes along the (001) direction.

Oxygen content and transition metal oxidation state determination

The mean (Co, Fe) oxidation state and therefore the oxygen content at room temperature were obtained by Mohr salt titration and are reported for $x \leq 1.5$ in Table 1. At increasing iron amount, the oxygen content $5 + \delta$ increases resulting in a decrease of the oxygen vacancy concentration $(1 - \delta)$ (the maximum oxygen concentration being 6 for the double perovskites).

The Mössbauer spectra of $PrBaCo_{2-x}Fe_xO_{5+\delta}$ ($x = 0.5$, 1 and 1.5) compounds recorded at room temperature are shown in Fig. 2. Their general profile can be fitted using two quadrupole doublets, except for $PrBaCo_{1.5}Fe_{0.5}O_{5+\delta}$ where a third one is required. A first conventional fit performed using Lorentzian quadrupole doublets leads to large line width values, which suggests the existence of a distribution of quadrupole splittings and therefore a distribution of local iron environments. The Mössbauer spectra were then fitted considering two or three distributions of quadrupole splittings with a constant value of the ^{57}Fe isotope line width ($\Gamma = 0.25$ mm s^{-1}) and the isomer shift fixed at the value determined in the first fit. The characteristic parameters, *i.e.* the isomer shift (IS) and the mean quadrupole splitting (Δ^*), are given for $x = 0.5$, 1 and 1.5 in Table 2.

The isomer shift of the predominant distribution, IS = 0.28 mm s^{-1}, is assigned to an iron ion in distorted octahedral

Table 1 Lattice parameters, transition metal oxidation state and oxygen content at room temperature in air for $PrBaCo_{2-x}Fe_xO_{5+\delta}$ materials (x = 0, 0.5, 1, 1.5 and 2)

Compounds	Space group	a (Å)	b (Å)	c (Å)	V (Å^3)	Oxidation state Co/Fe	Oxygen content $5+\delta$
$PrBaCo_2O_{5+\delta}$	*Pmmm*	3.902(1)	3.906(1)	7.639(2)	58.21(1)	3.30+	5.80
$PrBaCo_{1.5}Fe_{0.5}O_{5+\delta}$	*Pmmm*	3.913(2)	3.916(1)	7.670(2)	58.76(1)	3.41+	5.91
$PrBaCoFeO_{5+\delta}$	*Pmmm*	3.913(2)	3.920(2)	7.735(8)	59.32(1)	3.45+	5.95
$PrBaCo_{0.5}Fe_{1.5}O_{5+\delta}$	*Pm*$\bar{3}$*m*	3.917(2)	—	—	60.10(1)	3.48+	5.98
$PrBaFe_2O_{5+\delta}$	*Pm*$\bar{3}$*m*	3.938(2)	—	—	61.02(1)		
+Impurities	*Pbnm*	5.481(4)	5.533(4)	7.804(2)			

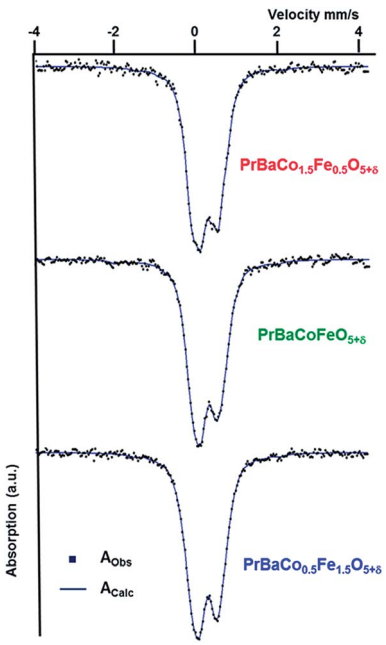

Fig. 2 Mössbauer spectra obtained for $PrBaCo_{2-x}Fe_xO_{5+\delta}$ (x = 0.5, 1 and 1.5) at 293 K in the velocity range [−4; +4 mm s^{-1}].

sites (with regard to the high values of the mean quadrupole splitting Δ* depending on the x value) and with an intermediate oxidation state Fe^{3-4+} related to a hopping phenomenon. Considering a linear variation between Fe^{3+} (IS = 0.36 mm s^{-1}) and Fe^{4+} (IS = −0.02 mm s^{-1}), one can assign this site (IS = 0.28 mm s^{-1}) to iron with an oxidation state of 3.24+ (24% in Fe^{4+}). In addition, due to a relatively low oxygen vacancy concentration in these compounds and the large occurrence of this distribution, the assumption of Fe^{3+} in pentahedral sites has been ruled out.

The minor site IS = −0.02 mm s^{-1}, is assigned to Fe^{4+} in distorted octahedral sites. For $PrBaCo_{1.5}Fe_{0.5}O_{5+\delta}$ the third site with an isomer shift IS = 0.36 mm s^{-1} and a quadrupole splitting Δ = 0.38 mm s^{-1} is characteristic of Fe^{3+} in octahedral sites.

It is interesting to note (Table 2) that the calculated oxidation state of iron in $PrBaCo_{2-x}Fe_xO_{5+\delta}$ compounds is rather constant and equal to $Fe^{3.35+}$. Consequently, the oxidation of these double perovskite oxides at increasing iron concentration directly results from the only oxidation of Co^{3+} to Co^{4+}. For $PrBaCo_{0.5}Fe_{1.5}O_{5+\delta}$, cobalt ions reach an oxidation state of 4+, Table 2.

As no significant modification of the iron environment is observed *vs.* the iron content, the loss of the BaO and PrO_δ ordering for $x > 1$ can be due to the low amount of oxygen vacancies, which prevents the rare earth arrangement in planes with a lower coordination number. This assumption is supported by the aforementioned non-ordering of x = 0.5 and 1 compounds after sintering at 1100 °C (*cf.* ESI, Fig. S1†), which provides less oxygen vacancies than the sintering at 1200 °C.

The thermal dependence of the oxygen content of $PrBaCo_{2-x}Fe_xO_{5+\delta}$ with δ = 0, 0.5, 1 and 1.5 was measured by TGA in air and under pO_2 = 0.01 bar (Fig. 3). The transition metal substitution does not cause major modifications in the oxygen content evolution *vs.* temperature and pO_2. However, a slight decrease of the relative variation of the oxygen content $\frac{(5+\delta)_{RT}-(5+\delta)_T}{(5+\delta)_{RT}}$, *i.e.* of the oxygen exchange with the

Table 2 Mössbauer parameters for $PrBaCo_{2-x}Fe_xO_{5+\delta}$ oxides (x = 0.5, 1.0 and 1.5) recorded at 293 K

Compounds	IS (mm s^{-1})	Γ (mm s^{-1})	Δ (mm s^{-1})	Distribution	%	%Fe^{4+}	%Co^{4+}
$PrBaCo_{1.5}Fe_{0.5}O_{5+\delta}$	0.28	0.25	0.70	Fe^{4+}/Fe^{3+} [Oh] hopping	39	34	51
	−0.02	0.25	0.33	Fe^{4+} [Oh]	24		
	0.36	0.25	0.38	Fe^{3+} [Oh]	37		
$PrBaCoFeO_{5+\delta}$	0.28	0.25	0.56	Fe^{4+}/Fe^{3+} [Oh] hopping	86	36	64
	−0.02	0.25	0.73	Fe^{4+} [Oh]	14		
$PrBaCo_{0.5}Fe_{1.5}O_{5+\delta}$	0.28	0.25	0.63	Fe^{4+}/Fe^{3+} [Oh] hopping	83	35	100
	−0.02	0.25	0.54	Fe^{4+} [Oh]	17		

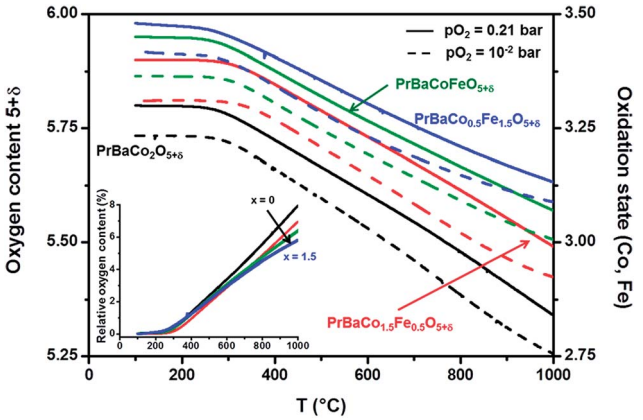

Fig. 3 Thermal dependence of the oxygen content $5+\delta$ for $PrBaCo_{2-x}Fe_xO_{5+\delta}$ materials ($x = 0$, 0.5, 1 and 1.5) under 0.21 (solid lines) and 0.01 (dashed lines) bar of O_2. In the inset is given the relative oxygen content evolution in % under air.

atmosphere, is observed at increasing iron concentration, as seen in the inset of Fig. 3.

Electrical transport properties

Fig. 4 shows the temperature dependence of the electrical conductivity and of the Seebeck coefficient (α) from room temperature up to 800 °C. The results are analysed with regard to whether the oxygen content is constant or not (see Fig. 3); indeed the measurements at high temperature on samples with changing oxygen stoichiometry only represent a specific piece of information at $[T_i, \delta_i]$ and obviously do not account for the full temperature dependence of a given compound.

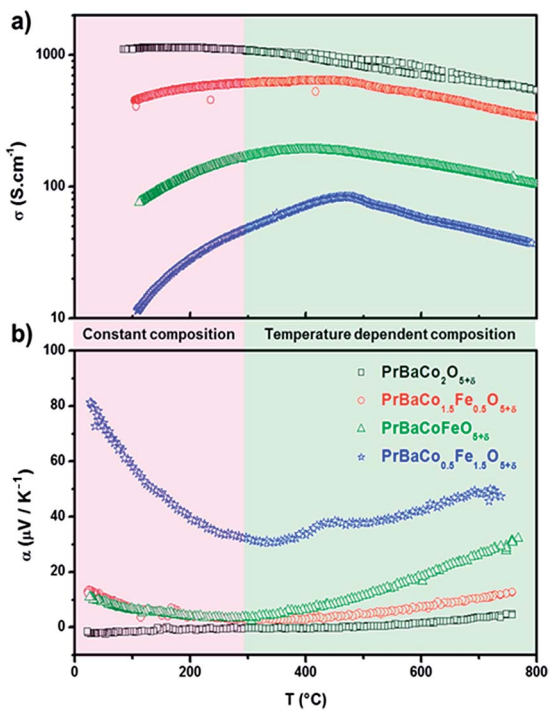

Fig. 4 Thermal variation in air of: (a) the electrical conductivity, (b) the Seebeck coefficient of $PrBaCo_{2-x}Fe_xO_{5+\delta}$ oxides ($x = 0$, 0.5, 1.0 and 1.5).

In the steady oxygen stoichiometry domain, below 280 °C, the conductivity is decreasing with the iron content x while, accordingly, the thermopower is globally increasing. In the same time, the conductivity changes from a metallic behaviour to an activated one; the metal to semiconducting transition appears quite early for $x < 0.5$. This transition is associated with a change in the dominant carriers going from electrons in the metallic region ($\alpha < 0$) to holes in the semiconducting one ($\alpha > 0$). The continuous increase of the activation energy determined from the conductivity data with the iron content strongly suggests the localization of the carriers, *i.e.* a loss of covalence as the substitution rate increases; such a picture is consistent with the increase of the thermopower. The activation energy of the conductivity ($x \geq 0.5$) actually increases linearly with x ($E_a \approx 30$, 83 and 143 meV for $x = 0.5$, 1 and 1.5 respectively), which allows refining a transition from a metal to a semiconductor at *ca.* $x \sim 0.24$ by zeroing this linear trend. Using the information in Table 1 to extrapolate the oxygen content at this value, the transition would occur for an average oxidation state of the transition metals of about 3.35 ($Co^{3+}/Co^{4+} \approx 2$). This value coincides with the actual average oxidation state of iron in the series (*vide infra*), suggesting that when the average oxidation state of cobalt is lower than that of iron the compound tends to be metallic while it is otherwise semiconducting. It is further interesting to note that the activation energies calculated from the thermopower are substantially lower ($E_N \approx 9$, 5 and 32 meV for $x = 0.5$, 1 and 1.5, respectively, where N refers to the carrier creation) than the ones calculated from the electric conductivity ($E_a = E_N + E_\mu$) evidencing a non-negligible activation of the mobility (μ) in this family of compounds ($x > 0$).

Above 280 °C, all the compounds begin to continuously lose oxygen. This reduction impacts on the electronic properties that now smoothly change with both the temperature and δ.

In the case of iron based compounds, as the temperature increases, δ increases and the average oxidation state of the transition metals decreases resulting in the decrease of the concentration of holes. The data can then reasonably be interpreted as resulting from the competition between the decrease in carrier concentration due to the reduction (*i.e.* oxygen loss) and the increase of their mobility which is thermally activated. The balance of the two contributions is evidenced by the inversion of the temperature dependence of the conductivity and one should care not to interpret this upturn as a semiconductor to metallic regime as each data point actually relates to a different compound (*i.e.* with different compositions). From our data, the balance temperature occurs in the region 400–470 °C: it increases with the iron content, x, and simultaneously the upturn is sharper. This is related to the fact that the mobility increases much slower as x increases and struggles more to compensate for the loss of carriers due to the decrease in δ.

In the case of the iron free compound the conductivity also decreases in the high temperature region but the dominant carriers change from electron to holes. This change in the nature of the carriers could mark the limit when the defect

concentration is too high to keep a metallic behaviour and actually signs a transition to a semiconducting state with a smooth drift of the chemical potential below the conduction band. Converting $\alpha(T)$ and $\delta(T)$ data sets into $\alpha(\delta)$ (Fig. 5) leads to finding a limit for the iron free compound at $\delta \approx 0.7$, *i.e.* a ratio of $Co^{3+}/Co^{4+} \approx 4$–5. Combining the results for the iron series and the iron free compound, the range of oxygen content allowing metallicity is about 5.7–5.85.

Oxygen diffusion and ionic conductivity determination

Values of the oxygen diffusion D^* and surface exchange k^* coefficients of double perovskites $LnBaCo_2O_{5+\delta}$ (with Ln = Pr and Gd) were previously reported.[19,27,28] However, a discrepancy between these values as high as two orders of magnitude was found, due to difficulties in obtaining dense pellets (d > 95%). Whereas the role of the rare earth/barium ordering and the subsequent localization of oxygen vacancies was studied by molecular dynamics,[29,30] nothing is known concerning the role of the transition metal in oxygen diffusivity in double perovskite oxides. Thus, the D^* and k^* coefficients have not yet been reported for iron substituted double perovskites.

Two different methods were used for determining these coefficients:

- The Electrical Conductivity Relaxation (ECR) in the 600–800 °C temperature range for $x = 0$ and 0.5 compositions. Typical ECR profiles obtained between air and 0.01 bar of oxygen at 650 °C are shown in Fig. 6a for $PrBaCo_2O_{5+\delta}$.

- The Isotopic Exchange Depth Profile coupled with Secondary Ion Mass Spectrometry (IEDP-SIMS) at 600 °C and 500 °C for $x = 0$ composition. A typical ^{18}O profile is given in Fig. 6b as well as the ^{59}Co, ^{16}O and ^{18}O mappings obtained by IEDP-SIMS analyses for $PrBaCo_2O_{5+\delta}$ (additional information is reported in Fig. S2†).

As described above, even though dense pellets of $PrBaCo_{2-x}Fe_xO_{5+\delta}$ (x = 0–1.5) were prepared with densities larger than 94%, no reliable diffusion profiles could be obtained for $x = 1$ and 1.5 compositions owing to the presence of pores and the determination of D^* and k^* coefficients was not possible for these compositions (Fig. S3†).

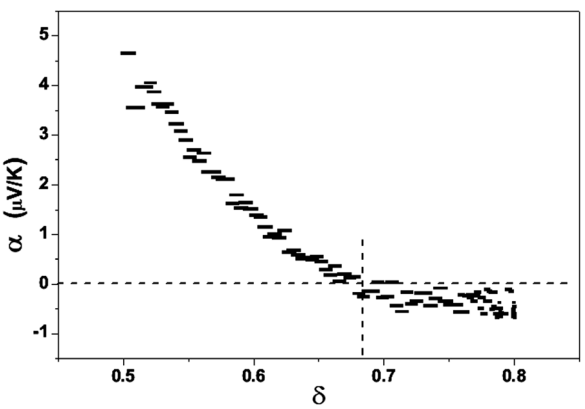

Fig. 5 Variation of the Seebeck coefficient *vs.* δ for $PrBaCo_2O_{5+\delta}$ in air.

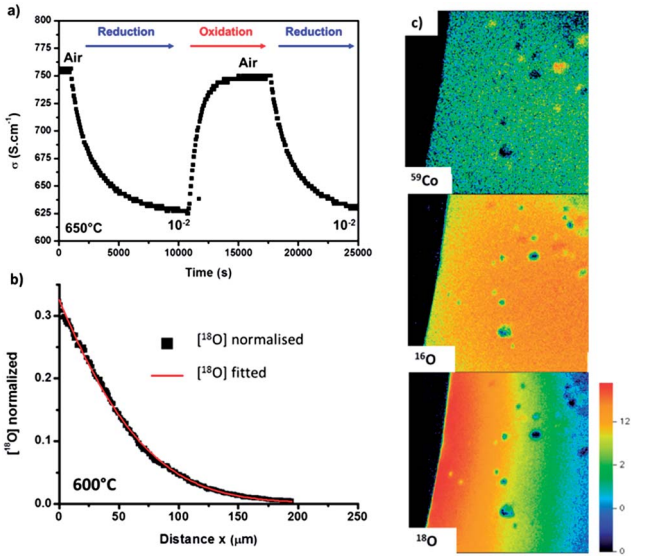

Fig. 6 (a) Typical electrical conductivity relaxation profiles for $PrBaCo_2O_{5+\delta}$ at 650 °C between 0.21 and 10^{-2} bar O_2, (b) ^{18}O diffusion profile (c) ^{59}Co, ^{16}O and ^{18}O mappings obtained by IEDP-SIMS analysis for $PrBaCo_2O_{5+\delta}$ at 600 °C.

While the isotopic oxygen diffusion and the surface exchange coefficients D^* and k^* are directly extracted from the refinement of the ^{18}O profiles of the IEDP-SIMS analysis, they can also be calculated starting from the D_{chem} and k_{chem} coefficients obtained by fitting the ECR profiles during the oxidation process (0.01 to 0.21 bar), using the following relationships:[31,32]

$$D^* = D_{chem}/\gamma \quad (6)$$

$$k^* = k_{chem}/\gamma \quad (7)$$

where γ is a thermodynamic factor:

$$\gamma = \frac{1}{2}\frac{\partial \ln(pO_2)}{\partial \ln(C_O)} \quad (8)$$

and C_O the oxygen concentration in the oxide calculated from TGA measurements reported in Fig. 3 (D_{chem}, k_{chem} and γ are provided in ESI Table S1†). The thermodynamic factors obtained are close to the one obtained by Wang *et al.* for $La_{0.5}Sr_{0.5}CoO_{3-\delta}$ (~100 to 120 in the temperature range).[24] Thus it can be considered to be in the linear model of oxygen exchange kinetics.

The D^* and k^* coefficients measured either by ECR or IEDP-SIMS analysis are plotted in Fig. 7 for $x = 0$ and 0.5 compositions. For comparison, the data for $x = 0$ reported by Burriel *et al.*[27] in the 300–700 °C temperature range are also given.

For $x = 0$, at 600 °C, both methods give similar coefficient values that are also in rather good agreement with those reported by Burriel *et al.*[27] For T < 600 °C, no reliable ECR profiles could be obtained and the value of the k^* coefficient obtained by IEDP-SIMS at 500 °C largely deviates from the value of these authors. One must notice that the ^{18}O diffusion observed on the SIMS map in Fig. S2† is not homogeneous on the surface of the sample, which could explain the large

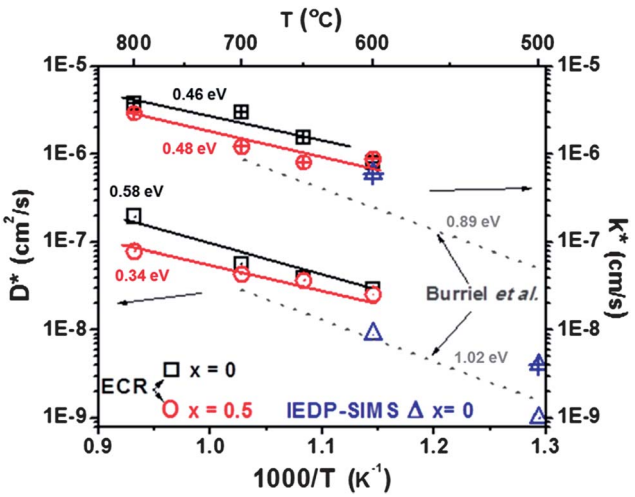

Fig. 7 Evolution *vs.* 1000/*T* of oxygen diffusion coefficient *D** and surface exchange coefficients *k** measured by ECR (□, ○) and IEDP-SIMS (Δ) for $PrBaCo_2O_{5+\delta}$ (black, $x = 0$) and $PrBaCo_{1.5}Fe_{0.5}O_{5+\delta}$ (red, $x = 0.5$) compared to coefficients obtained by Burriel *et al.* for $PrBaCo_2O_{5+\delta}$ (dashed lines).[27]

deviation observed at 500 °C for the *k** values of our study and of the one of Burriel *et al.*[27] Thus, this value must be considered as doubtful. Furthermore, the activation energies are slightly smaller than those found by these authors, which have been determined in a low temperature range. However, they are in agreement with the E_A value previously calculated or measured for the $GdBaCo_2O_{5+\delta}$ double perovskite.[27–30,33] This could be explained by a change in the value of the activation energy *versus* temperature, as previously discussed.[27] Though those coefficients are one order of magnitude lower than those reported for the best MIEC oxide, $Ba_{0.5}Sr_{0.5}Co_{0.8}Fe_{0.2}O_{3-\delta}$, they are two orders of magnitude larger than those of the $La_{0.6}Sr_{0.4}Fe_{0.8}Co_{0.2}O_{3-\delta}$ cubic perovskite.[34,35] In addition, they are of the same order of magnitude as the oxygen over-stoichiometric $Pr_2NiO_{4+\delta}$ oxide.[36]

Interestingly, the substitution of 25% of cobalt by iron does not significantly modify *D** and *k** coefficients.

As stated above, using MIEC oxides as H^+-SOFC cathodes, the ORR and water formation do not necessarily occur at the same place but are linked by the oxygen vacancy filling/formation process.[14] The oxygen diffusion can thus be a limiting process: therefore, the ionic conductivity of $PrBaCo_{2-x}Fe_xO_{5+\delta}$ (for $x = 0$ and 0.5) was calculated using the relationship:

$$\sigma_i = 2e\mu_{O^{2-}}[O^{2-}] \quad (9)$$

and the Nernst–Einstein equation:

$$\mu_{O^{2-}} = \frac{2e}{kT} D_{O^{2-}} \quad (10)$$

with e, the elementary charge, $[O^{2-}]$ the oxygen concentration and $\mu_{O^{2-}}$ the oxygen mobility. $D_{O^{2-}}$ is the oxygen diffusion coefficient correlated with the isotopic oxygen diffusion coefficient *D** by a correlation factor *f* equal to 0.69 for perovskites (direct oxygen diffusion through vacancies).[37] The oxygen concentration is given by the relationship: $[O^{2-}] = N/V_M$, N being the number of oxygen atoms per formula and $V_M = V/Z$, the volume of the unit cell at a given temperature, divided by the number of formula units (*cf.* ESI† for more details). Therefore, the thermal expansion coefficient (TEC) is required: it was assumed to be identical and equal to 20×10^{-6} K^{-1} for both $x = 0$ and 0.5.[25,40] The calculated ionic conductivities at 600 °C are given in Table 3 and are compared with the ionic conductivities of the two usual oxygen ion conductors used as SOFC electrolytes: $Ce_{0.9}Gd_{0.1}O_{2-\delta}$ (CGO10) and $Zr_{0.92}Y_{0.08}O_{2-\delta}$ (8YSZ).[38,39] The $O_{2\neg}$ conductivity for $PrBaCo_{2-x}Fe_xO_{5+d}$ with $x = 0$ and 0.5 are of the same order of magnitude, ~2 to 3 × 10^{-2} S cm^{-1} at 600 °C, as well as they are of the same order of magnitude as the protonic conductivity of the BCY10 electrolyte used in this study, 1.6 × 10^{-2} S cm^{-1} at 600 C.[41] As the value of the O^{2-} conduction of double perovskites with $x = 0$ and 0.5 is above one half of the value of the protonic conduction in the BCY10 electrolyte and according to the water formation reaction at the cathode (eqn (3)), one can thus consider that the ionic conductivity of these two oxides will not limit the ORR and water formation kinetics.

Electrochemical study

Electrochemical Impedance Spectroscopy (EIS) measurements. The electrochemical properties of the $PrBaCo_{2-x}Fe_xO_{5+\delta}$ materials used as oxygen electrodes deposited on $BaCe_{0.9}Y_{0.1}O_{2.95}$ electrolyte pellets were studied by Electrochemical Impedance Spectroscopy (EIS). The electrodes were sintered in different conditions in order to obtain microstructures with similar porosity (~30%) and a good adherence: at 1100 °C for 1 hour ($x = 0$), 1100 °C for 2 hours ($x = 0.5$), 950 °C for 1 hour ($x = 1$) and 1050 °C for 1 hour ($x = 1.5$). SEM images collected after the electrochemical studies are provided in the ESI (Fig. S4†). They exhibit almost identical microstructures for the four compounds.

The impedance diagrams (see a typical diagram in the ESI, Fig. S5†) were fitted with an equivalent circuit made of three resistance–constant phase elements in parallel associated in series, each one being assigned to a specific electrochemical phenomenon. On the basis of previous results reported for O^{2-}-SOFC cathode materials,[9,12] the first arc in the high frequency (HF) range is assigned to the electrolyte response. The second and third elements, in the middle (MF) and low frequency (LF)

Table 3 Ionic conductivity of $PrBaCo_2O_{5+\delta}$ calculated under air at 600 °C compared to ionic O^{2-} conductivity of $Ce_{0.9}Gd_{0.1}O_{2-\delta}$ and $Zr_{0.92}Y_{0.08}O_{2-\delta}$ electrolytes and to protonic conductivity of $BaCe_{0.9}Y_{0.1}O_{3-\delta}$.[38,39,41]

Compounds	Ionic (O^{2-} or H^+) conductivity at 600 °C under air (S cm^{-1})
$PrBaCo_2O_{5+\delta}$	2.9×10^{-2}
$PrBaCo_{1.5}Fe_{0.5}O_{5+\delta}$	2.4×10^{-2}
$Ce_{0.9}Gd_{0.1}O_{2-\delta}$	5×10^{-2}
$Zr_{0.92}Y_{0.08}O_{2-\delta}$	6×10^{-3}
$BaCe_{0.9}Y_{0.1}O_{3-\delta}$	1.6×10^{-2}

ranges are attributed to the ionic transfer at the electrolyte/electrode interface and to the electrode reaction, respectively.

Arrhenius plots of the polarization resistances, $R_p = R_{MF} + R_{LF}$, of the $PrBaCo_{2-x}Fe_xO_{5+\delta}$ electrodes, measured under wet air ($pH_2O = 0.03$ bar) and zero current conditions, are shown in Fig. 8. The electrode polarization resistance R_p increases with the iron content while the activation energies are similar and equal to ~1.3 eV for $x = 0$, 1 and 1.5; it is a bit larger for $PrBaCo_{1.5}Fe_{0.5}O_{5+\delta}$ (~1.5 eV). As seen in Fig. S4,† no significant change in the electrode morphology could be observed after electrochemical experiments and delamination issues can be excluded to explain these different activation energies.

Furthermore, the MF and LF resistances measured at 600 °C for each electrode are plotted *vs.* the electrical conductivity and the oxygen content $5+\delta$ (both extracted from the physical properties section) in Fig. 9a and b, respectively.

From data measured on different types of electrodes such as MIEC O^{2-}/e^-, composites or doped barium cerates, Peng *et al.* observed an increase in the LF resistance with decreasing electrical conductivity, which was assigned to the role played by the electronic conductivity in the $O_{(ads)}^-$ diffusion at the surface of the electrode.[6] In Fig. 9a, both MF and LF resistances increase with decreasing electrical conductivity, *i.e.* with increasing iron content. However, the electrical conductivity of these compounds remains larger than a dozen of S cm^{-1} at 600 °C and we do not believe that this is likely to be the governing parameter. It is worth noting that an increase of the MF resistance, associated with the electrode/electrolyte interface, is also observed. As no electron is exchanged at this interface, it confirms that the electronic conductivity is not the limiting physical parameter.

As discussed before, for these MIEC oxides the electronic conductivity is strongly correlated with the charge carrier concentration, *i.e.* with the modification of the transition metal oxidation states, which also is strongly correlated with the oxygen stoichiometry. Thus, a similar trend can be observed for the LF and MF resistance dependences with the oxygen content evolution measured under air at 600 °C (Fig. 9b). At decreasing oxygen vacancy concentration, both resistances associated with the electrolyte/electrode interface and the ORR at the electrode/gas interface are increasing. No effect of D^* and k^* can be expected for $x = 0$ and 0.5 compositions as they are similar at 600 °C (*cf.* Fig. 7).

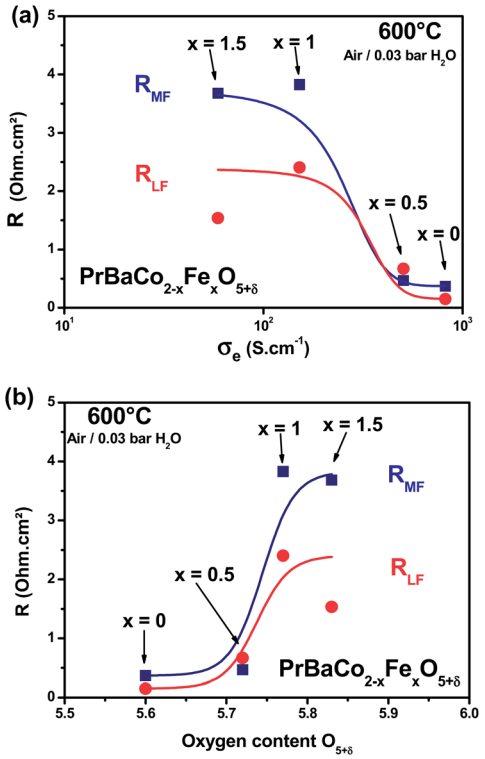

Fig. 9 Variation of the Middle Frequency (MF) and Low Frequency (LF) resistances of $PrBaCo_{2-x}Fe_xO_{5+\delta}$ electrodes ($x = 0$, 0.5, 1 and 1.5), at 600 °C under moist air (0.03 bar H_2O) as a function of: (a) the electrical conductivity and (b) the oxygen content (data from Fig. 3 and 4) (lines are guides for the eyes).

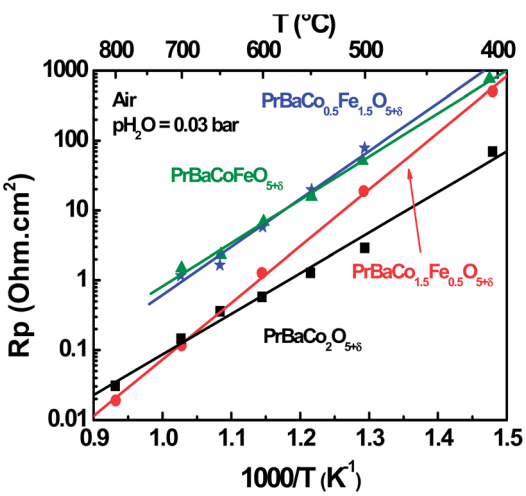

Fig. 8 Arrhenius plot of the polarization resistances measured under air/0.03 bar H_2O for $PrBaCo_{2-x}Fe_xO_{5+\delta}$ electrodes ($x = 0$, 0.5, 1 and 1.5).

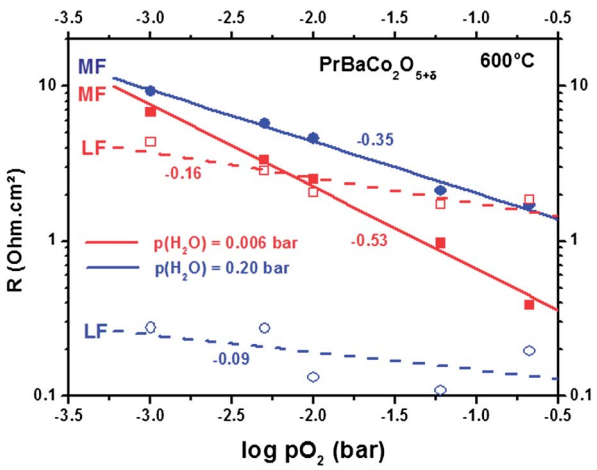

Fig. 10 pO_2 dependence of the middle frequency (solid symbols and lines) and low frequency (empty symbols and dashes) resistances for $PrBaCo_2O_{5+\delta}$ measured at 600 °C, under 0.06 bar (red) and 0.20 bar (blue) H_2O.

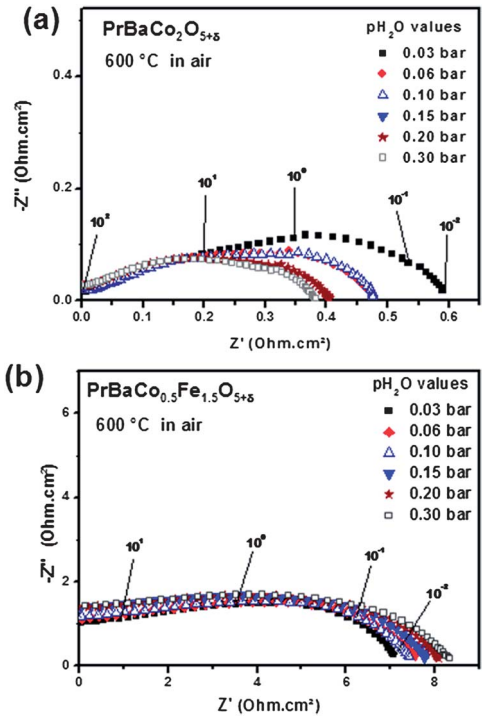

Fig. 11 Impedance diagrams recorded under air *vs.* pH_2O for a) $PrBaCo_2O_{5+\delta}$ and b) $PrBaCo_{0.5}Fe_{1.5}O_{5+\delta}$.

Determination of the rate determining step of the oxygen reduction reaction. As reported in Fig. 8, the substitution of cobalt by iron in double perovskite oxides leads to a strong decrease of the electrochemical performances of these electrodes. Previous measurements were performed under wet air; the next ones are carried out as a function of pH_2O, under various pO_2, with the aim to determine the Rate Determining Steps (RDS) of the oxygen reduction reaction and, possibly, to understand how the physical parameters of these double perovskites affect their electrochemical activity.

Measurements as a function of pO_2. EIS measurements were first performed for the $PrBaCo_2O_{5+\delta}$ electrode at 600 °C *vs.* pO_2 and under two different pH_2O, 0.006 and 0.20 bar, further denoted as a "dry" or "wet" atmosphere, respectively. The evolution of MF and LF resistances *vs.* pO_2 under a dry or wet atmosphere is shown in Fig. 10. The electrode reaction resistance (LF) largely decreases under the wet atmosphere, which would mean that the presence of steam improves the reaction at the surface of the electrode. The effect of water on the MF resistance is much weaker, this one being larger under the wet atmosphere.

The slope of the pO_2 dependence measured for the LF resistance is very small (the elementary steps as well as the partial pressure dependences are given in Table S2 in the ESI†); such a value of n means that oxygen is not involved in the RDS. Concerning the MF resistance, the n value is close to $-1/2$ or slightly smaller, which supposes that the RDS is the oxygen dissociation on the surface of the electrode. Under the wet atmosphere, the dependence is lower than 1/2 and even gets closer to 1/4: the negative effect of the presence of H_2O could result from the filling of oxygen vacancies under the wet atmosphere (eqn (5) in Table S2†). Decreasing the oxygen vacancy amount can then modify the RDS and limit the oxygen insertion (*cf.* eqn (3) in Table S2†).

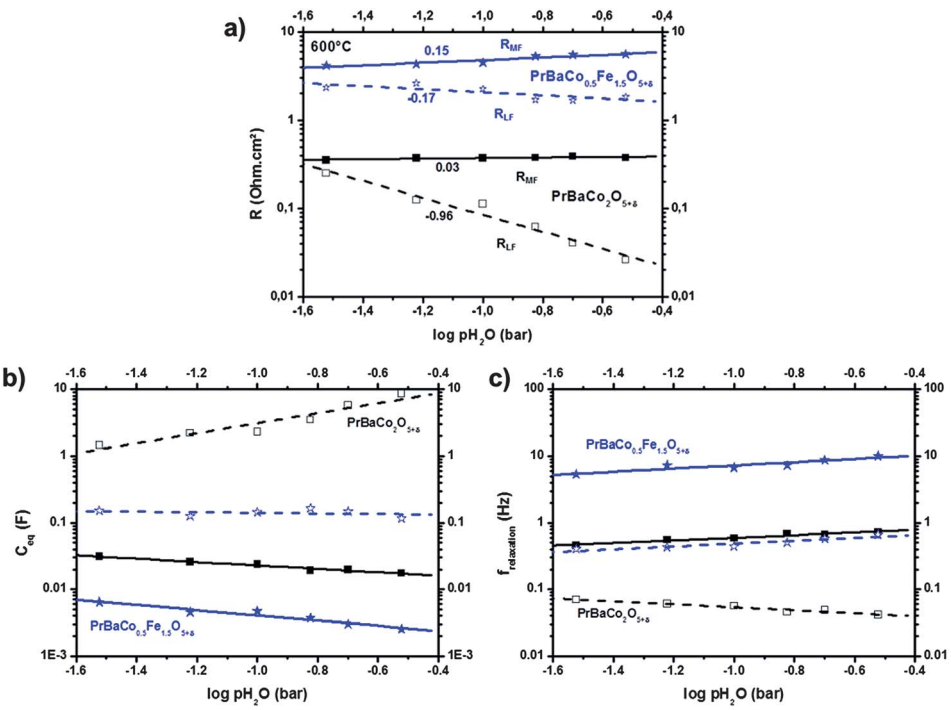

Fig. 12 Evolution under air, at 600 °C, *vs.* pH_2O of middle frequency (solid symbols and lines) and low frequency (open symbols and dashes) (a) resistances, (b) capacitances and (c) relaxation frequencies of $PrBaCo_2O_{5+\delta}$ (black) and $PrBaCo_{0.5}Fe_{1.5}O_{5+\delta}$ (blue).

Measurements as a function of pH_2O. EIS measurements were then performed at 600 °C under air *vs.* pH_2O for the end-members of the solid solution, $PrBaCo_2O_{5+\delta}$ and $PrBaCo_{0.5}Fe_{1.5}O_{5+\delta}$. The corresponding EIS diagrams are given in Fig. 11.

The ohmic contribution of the electrolyte has been subtracted in the diagrams; complex behaviours are observed. For $PrBaCo_2O_{5+\delta}$, the polarization resistance significantly decreases at increasing pH_2O. For $PrBaCo_{0.5}Fe_{1.5}O_{5+\delta}$, the polarization resistance increases with pH_2O which denotes a "blocking behaviour", *i.e.* a negative effect of water on the electrode reaction, and the value of the polarization resistance R_p is high. The dependences of the MF and LF resistances, capacitances and relaxation frequencies as a function of water content are given in Fig. 12. It clearly appears that the electrochemical behaviour of both oxides under pH_2O is different. A close to pH_2O^{-1} (0.96) dependence is measured for the LF resistance of $PrBaCo_2O_{5+\delta}$ (Fig. 12a), indicating the hydration of this cathode material in a water containing atmosphere. This corroborates the change in the pO_2 dependence observed under a wet atmosphere (Fig. 10), probably due to the filling of oxygen vacancies. The LF resistance of $PrBaCo_{0.5}Fe_{1.5}O_{5+\delta}$ is slightly modified by the presence of H_2O, which likely means that this oxide is not hydrated under the wet atmosphere. In contrast, the MF phenomenon observed for $PrBaCo_{0.5}Fe_{1.5}O_{5+\delta}$ characterizes a negative effect of water on the electrode phenomenon. Indeed, this iron containing oxide behaves as an O^{2-}/e^- MIEC oxide, devoid of protonic conduction whereas a proton is involved in the electrochemical process for $PrBaCo_2O_{5+\delta}$. This lack of protonic conduction could lead to water formation at the internal electrolyte/electrode interface, resulting in a significant increase of the MF resistance as previously mentioned. The electrochemical processes involved in both oxides thus do not take place at the same interface, which is further evidenced by the strong shift to lower capacitances and higher relaxation frequencies observed for $PrBaCo_{0.5}Fe_{1.5}O_{5+\delta}$, in comparison with $PrBaCo_2O_{5+\delta}$ (Fig. 12b and c). The MF resistance of $PrBaCo_2O_{5+\delta}$ is rather constant (Fig. 12a), which indicates a favourable transfer at the interface with the electrolyte and the formation of water on the surface of the electrode.

Discussion

The substitution of cobalt by iron in the double perovskites $PrBaCo_{2-x}Fe_xO_{5+\delta}$ induces oxidation of cobalt which affects the electrical conductivity, and subsequently a decrease of the oxygen vacancy concentration. This study highlighted that the electrochemical performances of these double perovskites as H^+-SOFC cathodes are also impacted by the changes in the physical properties. Regarding the electrochemical blocking effect observed under high pH_2O for $PrBaCo_{0.5}Fe_{1.5}O_{5+\delta}$, the oxygen content appears to be a key parameter for oxygen deficient MIEC oxides. Indeed, assuming that the hydration enthalpy of these oxides is relatively small compared to electrolyte materials, only a large amount of oxygen vacancies can allow these oxides to be hydrated under pH_2O. When the electrical conductivity is high enough (>several tens of S cm^{-1}), electron concentration is not a limiting factor for the oxygen reduction reaction occurring at the H^+-SOFC cathode, the reaction being then limited by the flux of protons coming from the electrolyte ($\sigma_{H^+(BCY10)} \sim 10^{-2}$ S cm^{-1} at 600 °C). It thus clearly appears that one condition required for oxygen deficient MIEC oxides to be suitable H^+-SOFC cathodes is to have high oxygen vacancy concentration. Even though the proton diffusion is probably limited in such MIEC oxides, their hydration ability provides hydroxyl groups which can be involved and favour the ORR mechanism.

Conclusion

Starting from $PrBaCo_2O_{5+\delta}$ known for its good electrochemical performance as a H^+-SOFC cathode, cobalt substitution by iron has been performed resulting in lowering of the electrical conductivity and increase of the oxygen content, *i.e.* decrease of the oxygen vacancy concentration. The electrochemical performances of these oxides have been measured under wet air and the dependence of MF and LF resistances on electrical conductivity and oxygen vacancy concentration was studied. The determination of RDS by EIS measurements carried out *vs.* pO_2 and pH_2O evidenced the proton to be involved in the electrochemical process for $PrBaCo_2O_{5+\delta}$ and the crucial role played by the oxygen vacancies concentration. The double perovskites showing a large amount of vacant sites for water insertion give the best electrochemical performances, owing to the delocalization of the water formation from the electrolyte/electrode interface to the electrode/gas interface. Low oxygen vacancy concentration leads to a blocking behaviour explained by the formation of water at the internal electrolyte/electrode interface.

Acknowledgements

The authors are grateful to EIfER, ADEME, Conseil Régional d'Aquitaine and ANR Agency (CONDOR-HPAC project) for their financial supports. They are also indebted to S. Pechev and F. Weill for their participation in the structural characterizations.

Notes and references

1 B. C. H. Steele and A. Heinzel, *Nature*, 2001, **414**, 345–352.
2 H. Iwahara, *Solid State Ionics*, 1996, **86–88**, 9–15.
3 T. Norby, M. Wildere, R. Glöckner and Y. Larring, *Dalton Trans.*, 2004, 3012–3018.
4 S. Tao, Q. Wu, D. Peng and G. Meng, *J. Appl. Electrochem.*, 2000, **30**, 153–157.
5 F. He, T. Wu, R. Peng and C. Xia, *J. Power Sources*, 2009, **194**, 263–268.
6 R. Peng, T. Wu, W. Liu, X. Liu and G. Meng, *J. Mater. Chem.*, 2010, **20**, 6218–6225.
7 R. Mukundan, P. Davies and W. Worrell, *J. Electrochem. Soc.*, 2001, **148**, A82–A86.
8 E. Fabbri, T.-K. Oh, S. Licoccia, E. Traversa and E. Wachsman, *J. Electrochem. Soc.*, 2009, **156**, B38–B45.
9 J. Dailly, S. Fourcade, A. Largeteau, F. Mauvy, J.-C. Grenier and M. Marrony, *Electrochim. Acta*, 2010, **55**, 5847–5853.

10 Y. Lin, R. Ran and Z. Shao, *Int. J. Hydrogen Energy*, 2010, **35**, 8281–8288.
11 K. Kravchyk, E. Quarez, M. Caldes, A. Le Gal La Salle and O. Joubert, *J. Power Sources*, 2011, **36**, 13059–13066.
12 A. Grimaud, F. Mauvy, J.-M. Bassat, S. Fourcade, L. Rocheron, M. Marrony and J.-C. Grenier, *J. Electrochem. Soc.*, 2012, **159**, B683–B694.
13 A. Grimaud, F. Mauvy, J.-M. Bassat, S. Fourcade, M. Marrony and J.-C. Grenier, *J. Mater. Chem.*, 2012, **22**, 16017–16025.
14 L. Wang, R. Merkle and J. Maier, *J. Electrochem. Soc.*, 2010, **157**, B1802–B1808.
15 P. Dordor, E. Marquestaut and G. Villeneuve, *Rev. Phys. Appl.*, 1980, **15**, 1607.
16 J. Crank, *The Mathematics of Diffusion*, Oxford Univ. Press, Oxford, 1975.
17 E. Boehm, J.-M. Bassat, P. Dordor, F. Mauvy, J.-C. Grenier and P. Stevens, *Solid State Ionics*, 2005, **176**, 2717–2725.
18 E. Boehm, J.-M. Bassat, M. C. Steil, P. Dordor, F. Mauvy and J.-C. Grenier, *Solid State Sci.*, 2003, **5**, 973–981.
19 G. Kim, S. Wang, A. J. Jacobson, L. Reimus, P. Brodersen and C. A. Mims, *J. Mater. Chem.*, 2007, **17**, 2500–2505.
20 F. Mauvy, J.-M. Bassat, E. Boehm, P. Dordor, J.-C. Grenier and J.-P. Loup, *J. Eur. Ceram. Soc.*, 2004, **24**, 1264–1269.
21 B. Ma, U. Balachandran, J.-H. Park and C. Segre, *Solid State Ionics*, 1996, **83**, 65–71.
22 I. Yasuda and M. Hishinuma, *J. Solid State Chem.*, 1996, **123**, 382–390.
23 W. Sitte, E. Bucher, A. Benisek and W. Preis, *Spectrochim. Acta, Part A*, 2001, **57**, 2071–2076.
24 S. Wang, A. Verma, Y. L. Yang, A. J. Jacobson and B. Abeles, *Solid State Ionics*, 2001, **140**, 125–133.
25 V. A. Cherepanov, T. V. Aksenova, L. Ya, L. Gavrilova and K. N. Mikhaleva, *Solid State Ionics*, 2011, **188**, 53.
26 R. D. Shannon, *Acta Crystallogr.*, 1976, **A32**, 751.
27 M. Burriel, J. Peña-Martínez, R. J. Chater, S. Fearn, A. V. Berenov, S. J. Skinner and J. A. Kilner, *Chem. Mater.*, 2012, **24**, 613–621.
28 I. D. Seymour, A. Tarancon, A. Chroneos, D. Parfitt, J. A. Kilner and R. W. Grimes, *Solid State Ionics*, 2012, **216**, 41–43.
29 D. Parfitt, A. Chroneos, A. Tarancon and J. A. Kilner, *J. Mater. Chem.*, 2011, **21**, 2183–2186.
30 J. Hermet, G. Geneste and G. Dezanneau, *Appl. Phys. Lett.*, 2010, **97**, 174102.
31 J. Maier, *Solid State Ionics*, 1998, **121**, 197–228.
32 H. Schmalzried, *Solid State Reactions*, Verlag Chemie, 2nd edn, 1981.
33 A. Tarancon, S. J. Skinner, R. J. Chatter, F. Hernandez-Ramirez and J. A. Kilner, *J. Mater. Chem.*, 2007, **17**, 3175–3181.
34 L. Wang, R. Merkle, J. Maier, T. Acartürk and U. Starke, *Appl. Phys. Lett.*, 2009, **94**, 071908.
35 A. Esquirol, J. A. Kilner and N. Brandon, *Solid State Ionics*, 2004, **174**, 63–67.
36 J.-M. Bassat, P. Odier, A. Villesuzanne, C. Marin and M. Pouchard, *Solid State Ionics*, 2004, **167**, 341–347.
37 J. Philibert, *Atom movements diffusion and mass transport in solids*, Les Editions de Physique, 1991.
38 O. H. Kwon and G. M. Choi, *Solid State Ionics*, 2006, **177**, 3057–3062.
39 D. Perez-Coll, E. Sanchez-Lopez and G. C. Mather, *Solid State Ionics*, 2010, **181**, 1033–1042.
40 Q. Zhou, F. Wang, Y. Shen and T. He, *J. Power Sources*, 2010, **195**, 2174–2181.
41 A. Grimaud, J.-M. Bassat, F. Mauvy, P. Simon, A. Canizares, B. Rousseau, M. Marrony and J.-C. Grenier, *Solid State Ionics*, 2011, **191**, 24–31.